

Signal-to-Noise Ratio Estimation in Passive Correlation-Based Imaging*

Josselin Garnier[†], George Papanicolaou[‡], Adrien Semin[§], and Chrysoula Tsogka[¶]

Abstract. We consider imaging with passive arrays of sensors using as illumination ambient noise sources. The first step for imaging under such circumstances is the computation of the cross correlations of the recorded signals, which have attracted a lot of attention recently because of their numerous applications in seismic imaging, volcano monitoring, and petroleum prospecting. Here, we use these cross correlations for imaging reflectors with travel-time migration. While the resolution of the image obtained this way has been studied in detail, an analysis of the signal-to-noise ratio (SNR) is presented in this paper along with numerical simulations that support the theoretical results. It is shown that the SNR of the image inherits the SNR of the computed cross correlations and therefore is proportional to the square root of the bandwidth of the noise sources times the recording time. Moreover, the SNR of the image is proportional to the array size. This means that the image can be stabilized by increasing the size of the array when the recorded signals are not of long duration, which is important in applications such as nondestructive testing.

Key words. correlation-based imaging, noise sources, resolution analysis, signal-to-noise ratio

AMS subject classifications. 35R30, 35R60, 78A46, 35L05

DOI. 10.1137/120875533

1. Introduction. We consider passive array imaging using as illumination ambient noise sources. We compute the cross correlations of the signals recorded at the array of sensors and form an image by backpropagating or migrating them to a region of interest containing reflectors. In this paper we assess the quality of such images in terms of several parameters that affect it. There are two types of analyses that must be carried out. The first is a resolution analysis of the imaging functional [11], and the second is an analysis of the signal-to-noise ratio (SNR), which is done in this paper. Our main result is that the SNR of the image is proportional $N_R\sqrt{BT}$ for an array of N_R sensors placed at a distance of half a central wavelength or more, with B the bandwidth of the noise sources and T the recording time. The analysis and the numerical simulations are carried out in two space dimensions, but the result

*Received by the editors May 1, 2012; accepted for publication (in revised form) March 11, 2013; published electronically June 6, 2013. The work of the third and fourth authors was partially supported by the European Research Council Starting grant, GA 239959, and the FP7-REGPOT-2009-1 project “Archimedes Center for Modeling, Analysis and Computation.”

<http://www.siam.org/journals/siims/6-2/87553.html>

[†]Laboratoire de Probabilités et Modèles Aléatoires & Laboratoire Jacques-Louis Lions, Université Paris VII, Site Chevaleret, 75205 Paris Cedex 13, France (garnier@math.univ-paris-diderot.fr). The work of this author was partially supported by ERC Advanced Grant Project MULTIMOD-267184.

[‡]Department of Mathematics, Stanford University, Stanford, CA 94305 (papanicolaou@stanford.edu). The work of this author was partially supported by AFOSR grant FA9550-11-1-0266.

[§]Institute of Applied and Computational Mathematics, FORTH, GR-70013 Heraklion, Greece (asemin@iacm.forth.gr).

[¶]Department of Applied Mathematics, University of Crete and IACM/FORTH, GR-71409 Heraklion, Greece (tsogka@tem.uoc.gr).

is the same in three dimensions. This result is interesting and perhaps unexpected because of the linear increase of the SNR of the image with the number of sensors, which can be closely spaced. Thus, when recording times are not very long, as may be the case in nondestructive testing, the stability of the image (its SNR) can be improved by increasing the size of the array.

Passive correlation-based imaging exploits the fact that information about the Green's function in the background medium can be obtained from cross correlations of noise signals. This was first shown experimentally in [20], where the authors observed that the Green's function in a closed cavity can be retrieved from passive noise recordings due to thermal noise. The analysis in [20] is based on the modal expansion of the displacement field. Another theoretical explanation of this phenomenon was given in [16] using stationary phase analysis. The precise result is that the derivative of the cross correlations of the recorded signals equals the symmetrized Green's function between the sensors. This can be obtained in open systems using the Helmholtz–Kirchhoff identity [10, 19], provided that the noise sources surround the region of interest. In the case of closed systems, i.e., cavities, the sources can be spatially localized provided the cavity is ergodic [1, 6].

The first application of these ideas to imaging was in helioseismology [7] and, more recently, in passive seismic imaging of the surface velocity of the earth [13, 15]. Other potential applications include volcano monitoring, petroleum prospecting, and structural health monitoring [17, 5, 18]. In this paper, motivated by applications in structural health monitoring, we study theoretically and numerically the quality of the image obtained by migrating cross correlations of noise recordings with a passive array of sensors. A schematic of the source, array, and reflector configuration is shown in Figure 1. The support of the ambient noise sources is limited to the grey region on the left of the image. The sources could be either natural noise sources (air, vibrations, etc.) or controlled ultrasonic sources generating noise signals on the surface of the structure under investigation. The array of passive sensors is depicted by triangles in Figure 1 and is assumed to be embedded in the structure. The black square represents a defect (hole, crack, etc.) that we wish to detect and image. The parameters used in our numerical simulations are given in section 5 and are chosen to be close to the experimental ones reported in [14], where the monitoring of aircraft fuselage and wing structures is considered.

Reflector imaging with ambient noise sources was first considered in [10], where it was shown that it can be done by migrating cross correlations of recorded signals. We refer the reader also to [12] for an experimental demonstration of passive correlation-based imaging of a buried scatterer. For the configuration of Figure 1, stationary phase analysis shows that the cross correlation of the signals recorded at a pair of sensors has a peak at the sum of the travel times between the sensors and the scatterer [10]. This is the same as for usual active array imaging, and therefore the Rayleigh resolution limits are valid [4]. This means that the cross range resolution for a linear sensor array with aperture a is given by $\lambda L_r/a$. Here L_r is the distance between the sensor array and the reflector, and λ is the central wavelength. The range resolution for broadband noise sources is given by $c_0 B^{-1}$, where c_0 is the speed of propagation and B is the bandwidth of the noise sources.

This paper is organized as follows. Using the wave equation, we formulate in section 2 wave propagation with noise sources and state the basic properties of cross correlations between



Figure 1. Schematic of passive array imaging with ambient noise sources: The grey region is the spatial support of the noise sources, the triangles are the sensors, and the square is the reflector.

signals recorded at different sensors in section 3. The imaging problem is presented in section 4, where we also briefly recall the resolution analysis. We carry out in detail the SNR analysis of the image. Our numerical results presented in section 5 are in very good agreement with the theory, illustrating both the imaging resolution limits and the SNR analysis.

2. Acoustic wave model with noise sources. To model wave propagation phenomena we consider the linear acoustic wave equation

$$(2.1) \quad \frac{1}{\rho(\mathbf{x})} \frac{\partial^2 u(t, \mathbf{x})}{\partial t^2} - \operatorname{div}(\mu(\mathbf{x}) \nabla u(t, \mathbf{x})) = n(t, \mathbf{x})$$

in two dimensions, $\mathbf{x} = (x, z)$, in a medium with $\rho(\mathbf{x}) = 1$ and $\mu(\mathbf{x})$ given by

$$(2.2) \quad \mu(\mathbf{x}) = c_0(\mathbf{x})^2.$$

Here $u(t, \mathbf{x})$ is the displacement field, and $c_0(\mathbf{x})$ is the smooth and known speed of sound in the background medium. In most of our simulations we assume that the propagation medium is homogeneous and therefore the velocity c_0 is constant. In (2.1) $n(t, \mathbf{x})$ models the noise sources. It is a zero-mean stationary (in time) random process with correlation function

$$(2.3) \quad E \{n(t_1, \mathbf{x}_1)n(t_2, \mathbf{x}_2)\} = \mathbb{F}(t_1 - t_2)K(\mathbf{x}_1)\delta(\mathbf{x}_1 - \mathbf{x}_2).$$

The process n is delta-correlated in space and K characterizes the spatial support of the sources. The time distribution of the noise is characterized by the correlation function $\mathbb{F}(t_1 - t_2)$. The Fourier transform of \mathbb{F}

$$\hat{\mathbb{F}}(\omega) = \int \mathbb{F}(t)e^{i\omega t} dt$$

is the power spectral density of the noise sources. The details of how we simulate the noise source $n(t, \mathbf{x})$ are given in Appendix A.

The solution of (2.1) in a homogeneous medium can be expressed in terms of the time-harmonic Green's function for the wave equation which in the two-dimensional case is given by

$$(2.4) \quad \hat{G}(\omega, \mathbf{x}, \mathbf{y}) = \frac{i}{4} H_0^{(1)}(\omega \mathcal{T}(\mathbf{x}, \mathbf{y})),$$

where $\mathcal{T}(\mathbf{x}, \mathbf{y}) = |\mathbf{x} - \mathbf{y}|/c_0$ is the travel time between points \mathbf{x} and \mathbf{y} and $H_0^{(1)}$ is the Hankel function of first type and zero order.

3. Cross correlations of noise signals. Let $u(t, \mathbf{x}_1)$ and $u(t, \mathbf{x}_2)$ be the solution of (2.1) at \mathbf{x}_1 and \mathbf{x}_2 , the locations of two sensors. The quantity that we compute in practice is the empirical cross correlation of these two signals over the time interval $[0, T]$ with time lag τ ,

$$(3.1) \quad C_T(\tau, \mathbf{x}_1, \mathbf{x}_2) = \frac{1}{T} \int_0^T u(t, \mathbf{x}_1)u(t + \tau, \mathbf{x}_2)dt.$$

Note that C_T , being a convolution, can be efficiently computed using the discrete Fourier transform (DFT), as we explain in Appendix B. What is important for imaging is that the empirical cross correlation C_T is a statistically stable quantity in the sense that for a large integration time T it is independent of the realization of the noise sources. More precisely, we have the following results (the first two items are proved in [10]).

1. The expectation of the empirical cross correlation C_T (with respect to the distribution of the sources) is independent of T :

$$(3.2) \quad \langle C_T(\tau, \mathbf{x}_1, \mathbf{x}_2) \rangle = C^{(1)}(\tau, \mathbf{x}_1, \mathbf{x}_2),$$

where the statistical cross correlation $C^{(1)}$ is given by

$$(3.3) \quad C^{(1)}(\tau, \mathbf{x}_1, \mathbf{x}_2) = \frac{1}{2\pi} \int \hat{D}(\omega, \mathbf{x}_1, \mathbf{x}_2) \overline{\hat{F}(\omega)} e^{-i\omega\tau} d\omega,$$

$$(3.4) \quad \hat{D}(\omega, \mathbf{x}_1, \mathbf{x}_2) = \int \overline{\hat{G}(\omega, \mathbf{x}_1, \mathbf{y})} \hat{G}(\omega, \mathbf{x}_2, \mathbf{y}) K(\mathbf{y}) d\mathbf{y},$$

and $\hat{G}(\omega, \mathbf{x}, \mathbf{y})$ is the time-harmonic Green’s function given by (2.4) when the medium is homogeneous.

2. The empirical cross correlation C_T is a self-averaging quantity:

$$(3.5) \quad C_T(\tau, \mathbf{x}_1, \mathbf{x}_2) \xrightarrow{T \rightarrow \infty} C^{(1)}(\tau, \mathbf{x}_1, \mathbf{x}_2),$$

in probability with respect to the distribution of the sources.

3. If the noise sources have Gaussian statistics, then the covariance of the empirical cross correlation C_T is

$$(3.6) \quad \begin{aligned} & \text{Cov}(C_T(\tau, \mathbf{x}_1, \mathbf{x}_2), C_T(\tau', \mathbf{x}_3, \mathbf{x}_4)) \\ &= \frac{1}{2\pi T} \int \hat{D}(\omega, \mathbf{x}_1, \mathbf{x}_3) \overline{\hat{D}(\omega, \mathbf{x}_2, \mathbf{x}_4)} \hat{F}(\omega)^2 e^{-i\omega(\tau' - \tau)} d\omega \\ &+ \frac{1}{2\pi T} \int \hat{D}(\omega, \mathbf{x}_1, \mathbf{x}_4) \overline{\hat{D}(\omega, \mathbf{x}_2, \mathbf{x}_3)} \hat{F}(\omega)^2 e^{-i\omega(\tau' + \tau)} d\omega \end{aligned}$$

when $BT \gg 1$ (here B is the bandwidth of the noise sources, i.e., the width of the power spectral density \hat{F}). Therefore, errors may occur when the averaging time is not sufficient to ensure that time averages approximate statistical mean values. The SNR of the cross correlation is proportional to \sqrt{T} . This error will propagate in the migration formula in reflector imaging.

4. Passive sensor imaging with cross correlations. In this section, we assume that the background medium is homogeneous or smoothly varying and that there is a point reflector embedded in the medium at \mathbf{z}_r . We consider an array of N_R passive sensors located at $(\mathbf{x}_j)_{1 \leq j \leq N_R}$. The recorded signals are denoted by $u(t, \mathbf{x}_j)$ for $1 \leq j \leq N_R$.

We consider here the configuration where the noise sources are spatially localized and the sensors are located between the sources and the reflectors (see Figure 1). This configuration is called daylight, and for this case the high-frequency analysis carried out in Appendix C shows that there is a peak in the cross correlation between the receivers \mathbf{x}_j and \mathbf{x}_l at the sum of travel times between \mathbf{x}_j and \mathbf{z}_r and between \mathbf{x}_l and \mathbf{z}_r . Using this result, the appropriate imaging functional migrates the array data with the sum of travel times to the search point \mathbf{z} :

$$(4.1) \quad \mathcal{I}^D(\mathbf{z}) = \sum_{j,l=1}^{N_R} C_T(\mathcal{T}(\mathbf{z}, \mathbf{x}_l) + \mathcal{T}(\mathbf{z}, \mathbf{x}_j), \mathbf{x}_j, \mathbf{x}_l).$$

4.1. Resolution analysis. We consider here the behavior of the mean of the imaging functional \mathcal{I}^D . Note that the empirical imaging functionals are equal to their means when the integration time T is very long so that $C_T = C^{(1)}$.

The resolution analysis of the daylight imaging functional is carried out in [11] when there is a point reflector at \mathbf{z}_r . The cross range resolution for a linear sensor array with aperture a is given by $\lambda L_r/a$. Here L_r is the distance between the sensor array and the reflector, and λ is the central wavelength. The range resolution for broadband noise sources is equal to $c_0 B^{-1}$, where B is the bandwidth of the noise sources (i.e., the width of the function $\hat{\mathbb{F}}$). The range resolution for narrowband noise sources is $\lambda L_r^2/a^2$. The peak of the imaging functional is obtained at $\mathbf{z} = \mathbf{z}_r$. It is independent of T , and the peak amplitude is proportional to N_R^2 in terms of the number of receivers N_R and proportional to $\int \hat{\mathbb{F}}(\omega) d\omega$ in terms of the power spectral density [11].

The resolution analysis [11] shows that the results obtained in the case of noise sources are basically the same as those obtained for array imaging with deterministic sources [3, 2] always under the hypothesis that the integration time T is long enough.

4.2. Fluctuation analysis. Here we consider the behavior of the variance of the imaging functional \mathcal{I}^D . This means that we study the fluctuations of \mathcal{I}^D when the integration time T is not long enough to ensure the validity of the self-averaging relation $C_T = C^{(1)}$.

When migrating the cross correlations, the fluctuations come from $C_T - C^{(1)}$, and we have

$$\begin{aligned} \text{Var}(\mathcal{I}^D(\mathbf{z})) &= \sum_{j,l,j',l'=1}^{N_R} \text{Cov}(C_T(\mathcal{T}(\mathbf{z}, \mathbf{x}_l) + \mathcal{T}(\mathbf{z}, \mathbf{x}_j), \mathbf{x}_j, \mathbf{x}_l), \\ &\quad C_T(\mathcal{T}(\mathbf{z}, \mathbf{x}_{l'}) + \mathcal{T}(\mathbf{z}, \mathbf{x}_{j'}), \mathbf{x}_{j'}, \mathbf{x}_{l'})) \\ &\simeq \sum_{j,l,j',l'=1}^{N_R} \text{Cov}(C_{T,0}(\mathcal{T}(\mathbf{z}, \mathbf{x}_l) + \mathcal{T}(\mathbf{z}, \mathbf{x}_j), \mathbf{x}_j, \mathbf{x}_l), \\ &\quad C_{T,0}(\mathcal{T}(\mathbf{z}, \mathbf{x}_{l'}) + \mathcal{T}(\mathbf{z}, \mathbf{x}_{j'}), \mathbf{x}_{j'}, \mathbf{x}_{l'})), \end{aligned}$$

where $C_{T,0}$ is the cross correlation of the signals recorded when there is no reflector. The last approximate equality comes from the fact that the fluctuations of the cross correlations due to the finite integration time are dominated by the contributions of the waves that have not interacted with the reflector (the waves scattered by the reflector are much weaker in our regime). Using (3.6) we find

$$(4.2) \quad \text{Var}(\mathcal{I}^D(\mathbf{z})) = V_I + V_{II},$$

$$(4.3) \quad V_I = \frac{1}{2\pi T} \int \hat{\mathbb{F}}(\omega)^2 \left[\sum_{j,l=1}^{N_R} e^{i\omega[\mathcal{T}(\mathbf{z},\mathbf{x}_l) - \mathcal{T}(\mathbf{z},\mathbf{x}_j)]} \hat{D}(\omega, \mathbf{x}_l, \mathbf{x}_j) \right] \times \left[\sum_{j,l=1}^{N_R} e^{-i\omega[\mathcal{T}(\mathbf{z},\mathbf{x}_l) - \mathcal{T}(\mathbf{z},\mathbf{x}_j)]} \hat{D}(\omega, \mathbf{x}_l, \mathbf{x}_j) \right] d\omega,$$

$$(4.4) \quad V_{II} = \frac{1}{2\pi T} \int \hat{\mathbb{F}}(\omega)^2 \left[\sum_{j,l=1}^{N_R} e^{i\omega[\mathcal{T}(\mathbf{z},\mathbf{x}_l) + \mathcal{T}(\mathbf{z},\mathbf{x}_j)]} \hat{D}(\omega, \mathbf{x}_l, \mathbf{x}_j) \right]^2 d\omega.$$

In order to estimate the order of magnitude of the variance, we assume hereafter an ideal situation in which the noise sources surround the region of interest and cover the surface of a large ball Ω that contains the reflector and the array. We will discuss (both with theoretical and numerical arguments) the robustness of the results later. In this ideal situation we can use the Helmholtz–Kirchhoff identity

$$\text{Im}(\hat{G}(\omega, \mathbf{x}_l, \mathbf{x}_j)) = \frac{\omega}{c_0} \int_{\partial\Omega} \overline{\hat{G}(\omega, \mathbf{x}_l, \mathbf{y})} \hat{G}(\omega, \mathbf{x}_j, \mathbf{y}) dS(\mathbf{y}),$$

which is an asymptotic identity that is valid when the radius of the ball Ω goes to infinity and which follows from the second Green's identity and the Sommerfeld radiation condition [10]. We get

$$(4.5) \quad V_I = \frac{c_0^2}{2\pi T} \int \frac{\hat{\mathbb{F}}(\omega)^2}{\omega^2} \left| \sum_{j,l=1}^{N_R} e^{i\omega[\mathcal{T}(\mathbf{z},\mathbf{x}_l) - \mathcal{T}(\mathbf{z},\mathbf{x}_j)]} \text{Im}(\hat{G}(\omega, \mathbf{x}_l, \mathbf{x}_j)) \right|^2 d\omega,$$

$$(4.6) \quad V_{II} = \frac{c_0^2}{2\pi T} \int \frac{\hat{\mathbb{F}}(\omega)^2}{\omega^2} \left[\sum_{j,l=1}^{N_R} e^{i\omega[\mathcal{T}(\mathbf{z},\mathbf{x}_l) + \mathcal{T}(\mathbf{z},\mathbf{x}_j)]} \text{Im}(\hat{G}(\omega, \mathbf{x}_l, \mathbf{x}_j)) \right]^2 d\omega.$$

If the medium is homogeneous, then

$$\text{Im}(\hat{G}(\omega, \mathbf{x}_l, \mathbf{x}_j)) = \frac{1}{4} J_0(\omega \mathcal{T}(\mathbf{x}_l, \mathbf{x}_j)),$$

where J_0 is the zero-order Bessel function. In the following we carry out calculations in two cases, and then we discuss the main results.

Case 1. If the distance between sensors is larger than the wavelength, then only the diagonal terms $j = l$ contribute to the expressions of V_I and V_{II} , which gives

$$(4.7) \quad V_I \simeq \frac{c_0^2}{32\pi T} \int \frac{\hat{F}(\omega)^2}{\omega^2} \left| \sum_{j=1}^{N_R} e^{i\omega 0} \right|^2 d\omega = \frac{c_0^2 N_R^2}{32\pi T} \int \frac{\hat{F}(\omega)^2}{\omega^2} d\omega,$$

$$(4.8) \quad V_{II} \simeq \frac{c_0^2}{32\pi T} \int \frac{\hat{F}(\omega)^2}{\omega^2} \left| \sum_{j=1}^{N_R} e^{2i\omega \mathcal{T}(z, \mathbf{x}_j)} \right|^2 d\omega,$$

which is smaller than V_I . More precisely,

$$V_{II} \simeq \frac{c_0^2}{32\pi T} \sum_{j,l=1}^{N_R} \int \frac{\hat{F}(\omega)^2}{\omega^2} e^{2i\omega[\mathcal{T}(z, \mathbf{x}_j) - \mathcal{T}(z, \mathbf{x}_l)]} d\omega = \frac{c_0^2}{16T} \sum_{j,l=1}^{N_R} \Psi\left(2[\mathcal{T}(z, \mathbf{x}_j) - \mathcal{T}(z, \mathbf{x}_l)]\right),$$

where Ψ is the inverse Fourier transform of $\omega \rightarrow \hat{F}(\omega)^2/\omega^2$, whose width is of the order of the bandwidth B . If the distance between sensors is larger than c_0/B , then only the diagonal terms $j = l$ contribute to the double sum, and we find

$$(4.9) \quad V_{II} \simeq \frac{c_0^2 N_R}{32\pi T} \int \frac{\hat{F}(\omega)^2}{\omega^2} d\omega.$$

Case 2. If the array is dense (i.e., the distance between sensors is smaller than the wavelength) and occupies the line $[-a, a]$, and the search point \mathbf{z} is at distance L with $L \gg a \gg \lambda$, then

$$\begin{aligned} \sum_{j,l=1}^{N_R} e^{i\omega[\mathcal{T}(z, \mathbf{x}_l) - \mathcal{T}(z, \mathbf{x}_j)]} \text{Im}(\hat{G}(\omega, \mathbf{x}_l, \mathbf{x}_j)) &\simeq \frac{N_R^2}{16a^2} \int_{-a}^a \int_{-a}^a e^{i\frac{\omega}{c_0} \frac{x^2 - y^2}{2L}} J_0\left(\frac{\omega}{c_0} |x - y|\right) dx dy \\ &\simeq \frac{N_R^2}{16a^2} \int_{-2a}^{2a} ds \int_{-a+|s|/2}^{a-|s|/2} du e^{i\frac{\omega}{c_0} \frac{us}{L}} J_0\left(\frac{\omega}{c_0} |s|\right) \\ &\simeq \frac{N_R^2}{4} \int_0^1 \frac{\sin\left(\frac{2\omega a^2}{c_0 L} s(1-s)\right)}{\frac{\omega a^2}{c_0 L} s} J_0\left(\frac{2\omega a}{c_0} s\right) ds \\ &\simeq \frac{N_R^2 c_0}{4a\omega} = \frac{N_R^2 \lambda}{8\pi a}, \end{aligned}$$

since $\omega a^2/(Lc_0) \ll \omega a/c_0$, $\omega a/c_0 \gg 1$, and $\int_0^\infty J_0(s) ds = 1$. This gives the following for noise sources with a power spectral density centered at λ :

$$(4.10) \quad V_I \simeq \frac{c_0^2 N_R^4}{128\pi^3 T} \frac{\lambda^2}{a^2} \int \frac{\hat{F}(\omega)^2}{\omega^2} d\omega,$$

$$(4.11) \quad V_{II} \simeq 0.$$

This formula is in continuation of the discrete case: if we (formally) apply it to the case of a linear array sampled at $\lambda/2$, i.e., $2a = N_R \lambda/2$, then one finds $V_I \simeq \frac{c_0^2 N_R^2}{8\pi^3 T} \int \frac{\hat{F}(\omega)^2}{\omega^2} d\omega$, which has the same order of magnitude as (4.7).

4.3. SNR analysis. Here we assume that the bandwidth B of the noise sources is smaller than their central frequency ω_0 , or we assume that the noise sources are broadband, but we filter the recorded signals to keep only the frequency components in a band centered at ω_0 with width B . Then, in terms of the bandwidth, the peak amplitude (that is proportional to $\int \hat{\mathbb{F}}(\omega) d\omega$) is proportional to B , and the variance of the fluctuations (that is proportional to $\int \frac{\hat{\mathbb{F}}(\omega)^2}{\omega^2} d\omega$) is proportional to B as well.

The previous results show that, when the receiver arrays are sampled at more than half a wavelength apart, the variance of the daylight imaging functional is proportional to $N_R^2 B/T$, while the peak amplitude is proportional to $N_R^2 B$ (and independent of T). Therefore, the SNR defined by

$$(4.12) \quad \text{SNR}^{\text{D}} = \frac{\langle \mathcal{I}^{\text{D}}(\mathbf{z}_r) \rangle}{\text{Var}(\mathcal{I}^{\text{D}}(\mathbf{z}))^{1/2}}$$

is proportional to

$$(4.13) \quad \text{SNR}^{\text{D}} \sim N_R \sqrt{BT}.$$

When the receiver arrays are densely sampled, then the variance of the daylight imaging functional is proportional to $N_R^4 (\lambda/a)^2 B/T$, and therefore the SNR is proportional to

$$(4.14) \quad \text{SNR}^{\text{D}} \sim \sqrt{BT} (a/\lambda).$$

4.4. Robustness of the results. Here we discuss the robustness of the results with respect to different kinds of perturbations.

Additive measurement noise. The method is very robust to additive measurement noise as it is based on the processing of the cross correlations of the recorded signals, and the calculations of the cross correlations naturally eliminate the additive noises which are uncorrelated for different receivers.

Source distribution. In the previous subsections the analysis is carried out under the hypothesis that the sources surround the region of interest and cover the surface of a ball. This allows us to apply the Helmholtz–Kirchhoff identity, which considerably simplifies the analysis. However, this hypothesis is not necessary for the results to be true. In the case of spatially localized source distributions, one can use other approaches such as a high-frequency analysis and the application of stationary phase arguments [10]. Furthermore, the forthcoming sections will present results from numerical simulations in the configuration of Figure 1, in which the sources are indeed spatially localized.

Medium noise. We assume in this paper that the background medium is known. It turns out that the method is sensitive to the knowledge of the background medium in the same way that Kirchhoff migration with active array data is. It is necessary to know the travel times between receivers and search points with an accuracy of the order of the wavelength; otherwise the main peak can be blurred and/or shifted.

5. Numerical simulations. In our numerical simulations, we solve the wave equation (2.1) with the source term

$$(5.1) \quad n(t, \mathbf{x}) = \sum_{s=1}^{N_S} g(\mathbf{x} - \mathbf{x}_s) f_s(t).$$

The signals $(f_s(t))_{1 \leq s \leq N_S}$ emitted by the point sources are independent and identically distributed (i.i.d.) stationary signals as described in Appendix A with the power spectral density $\hat{\mathbb{F}}(\omega)$ given by

$$(5.2) \quad \hat{\mathbb{F}}(\omega) = \exp\left(-\frac{(\omega - \omega_0)^2}{B^2}\right) + \exp\left(-\frac{(\omega + \omega_0)^2}{B^2}\right),$$

where ω_0 is the central angular frequency and B is the bandwidth. Our numerical setup is shown in Figure 1. Our simulation parameters are chosen to be close to the experimental values reported in [14], where the problem of monitoring aircraft fuselage and wing structures was considered. The spatial support of the ambient noise sources is limited in the grey region on the left of the image, and the sensors are denoted by triangles and are assumed to be embedded in the structure under control. The black square represents a defect (hole, crack, etc.) that we wish to detect and image.

In (5.2), $\omega_0 = 2\pi f_0$ and $B = 2\pi\Delta f_0$ with $f_0 = 500$ kHz and $\Delta f_0 = 106$ kHz. The function g is Gaussian,

$$g(\mathbf{x}) = \beta \exp(-\alpha|\mathbf{x}|^2),$$

with $\alpha = -\ln(10^{-6})/r^2$, $\beta = \sqrt{\alpha/\pi}$, and $r = \lambda/2$, and λ is the wavelength associated with the central frequency f_0 . The speed of propagation is $c_0 = 3$ km/s so that the wavelength $\lambda = c_0/f_0$ is equal to 6 mm.

To solve the wave equation (2.1) we use the code Montjoie (<http://montjoie.gforge.inria.fr/>). Montjoie is designed for the efficient solution of time-domain and time-harmonic linear partial differential equations using high-order finite element methods. This code is written mainly for quadrilateral/hexahedral finite elements; partial implementations of triangular/tetrahedral elements are provided. The equations solved by this code come from the “wave propagation” problems, particularly acoustic, electromagnetic, aeroacoustic, and elastodynamic problems. For the numerical examples considered in this paper we solve (2.1) in the time domain using seventh-order finite elements in space and fourth-order finite differences in time.

We added the computation of cross correlations and imaging functionals in Montjoie. For the Fourier transform, we use GSL Fourier transform [9] and/or FFTW [8], depending on what is installed (these two libraries are interfaced in Montjoie so that the user does not have to code depending on the library he uses).

The numerical setup for the daylight test case configuration is shown in Figure 1. We analyze in this subsection the SNR of the daylight imaging functional as a function of the number of receivers N_R , the recording time T , and the bandwidth B .

The considered domain is the rectangle $[0, 50\lambda] \times [-15\lambda, 15\lambda]$, with a square hole located at $[44\lambda, 46\lambda] \times [-\lambda, \lambda]$. The noise sources are made of $N_S = 200$ point sources located at $(\mathbf{x}_s)_{1 \leq s \leq N_S}$, which is a collection of random points belonging to $[0, 4\lambda] \times [-15\lambda, 15\lambda]$. We use $N_R = 61$ receivers \mathbf{x}_j located at $(5\lambda, (j - 31)\lambda/2)$ for $j \in \{1, \dots, N_R\}$.

To give a quantitative result on the image of the scatterer, we compute in this section the SNR as follows. Let $\overline{\mathcal{I}^D}(\mathbf{z})$ be the averaged absolute value of the image over a square of size $2\lambda \times 2\lambda$ centered at \mathbf{z} . The SNR is computed as

$$(5.3) \quad \text{SNR} = \frac{\overline{\mathcal{I}^D}(\mathbf{z}^*)}{\max_{\mathbf{z} \neq \mathbf{z}^*} \overline{\mathcal{I}^D}(\mathbf{z})},$$

where \mathbf{z}^* is the point where the image admits its maximal value and $\mathbf{z} \neq \mathbf{z}^*$ means that squares of size $2\lambda \times 2\lambda$ centered at \mathbf{z} and \mathbf{z}^* do not intersect.

SNR versus number of receivers. We record in Table 1 measured SNRs for different configurations of receivers, and we plot the associated daylight images in Figures 2 and 4.

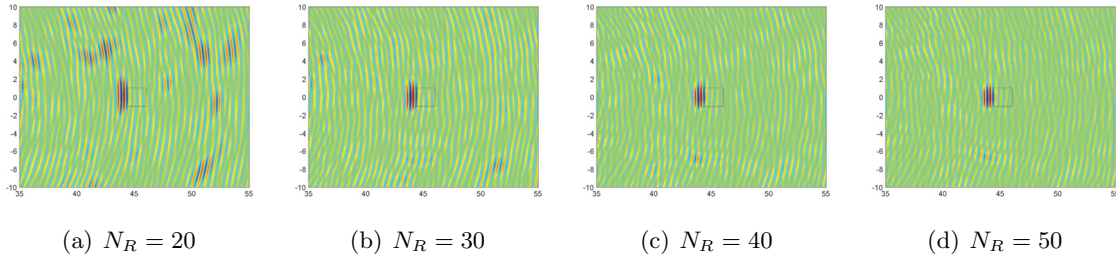


Figure 2. Daylight imaging with 200 sources. The distance between two consecutive receivers is $\delta = \lambda/2$. The recording time is $T = 480 \mu\text{s}$. The number of receivers is N_R .

The results in Table 1 and the images in Figure 2 show that the role of the number of receivers is twofold. First, as predicted by the resolution analysis, the cross range resolution improves by increasing the number of receivers, because this also means that the receiver array diameter increases. This is illustrated in Figure 2 by the focal spot on the scatterer that becomes tighter and gives a more accurate estimate of its size. At the same time, increasing N_R improves the SNR of the image, i.e., the amplitude of the ghosts in the image decreases, as predicted by the theoretical formula (4.13).

The results in Table 1 and the images in Figure 4 allow us to distinguish the two effects, cross range resolution enhancement and SNR reduction. Indeed they show that reducing the spacing between receivers while fixing the number of receivers does not modify the SNR (provided the distance between receivers remains larger than half a wavelength), as predicted by the theoretical formula (4.13), but it does reduce the cross range resolution, since the array diameter decays.

Table 1

Configurations and SNRs. The recording time is $T = 480 \mu\text{s}$. The spacing between receivers is δ .

Configuration of receivers	SNR
20 receivers, $\delta = \lambda/2$	1.74
30 receivers, $\delta = \lambda/2$	2.52
40 receivers, $\delta = \lambda/2$	3.06
50 receivers, $\delta = \lambda/2$	3.67
60 receivers, $\delta = \lambda/2$	4.31
20 receivers, $\delta = \lambda$	1.79
30 receivers, $\delta = \lambda$	2.37

We have also computed the regression equation of the measured SNR versus the number of receivers and plotted it in Figure 3. The regression equation is

$$(5.4) \quad \text{SNR} = 0.063N_R + 0.54,$$

with N_R the number of receivers. One can see that the SNR does linearly depend on the number of receivers, as predicted by the theory (see (4.13)).

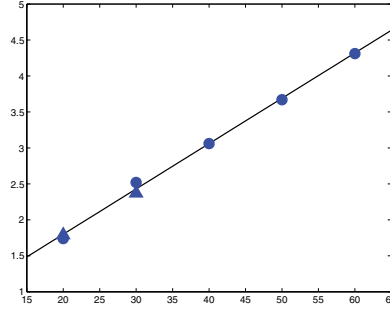


Figure 3. Plot of measured SNR versus number of receivers N_R (blue dots) and regression line (black line). Note that there are two markers at $N_R = 20$: They correspond to 20 receivers λ -apart from each other, or 20 receivers $\lambda/2$ -apart from each other. The same holds for $N_R = 30$. It can be seen that the SNR does not depend on the spacing between receivers (when it is larger than $\lambda/2$) but depends only on the number of receivers.

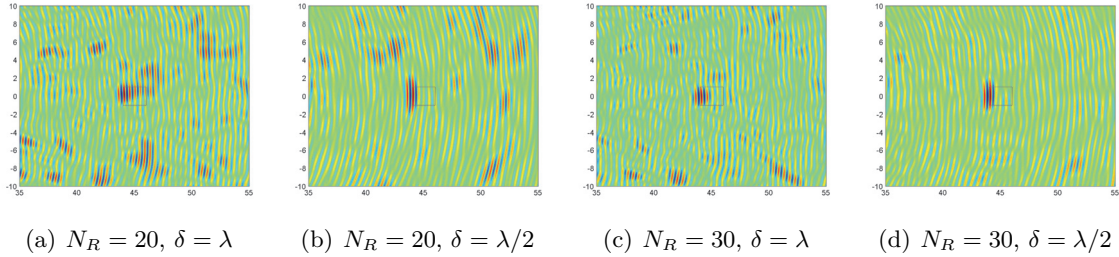


Figure 4. Daylight imaging with 200 sources. The recording time is $T = 480 \mu\text{s}$. There are N_R receivers, and the spacing between receivers is δ .

We note also that the number of ghosts in the image, i.e., the number of regions where the noise is high, depends on δ (see Figures 4(a) and 4(b)). The distance $\delta = \lambda/2$ gives a slightly better image, although this is not reflected at the SNR value as computed by (5.3).

SNR versus recording time. We record in Table 2 measured SNRs for different recording times T , and we plot the associated daylight images in Figure 5. We clearly see in Figure 5 that the quality of the image improves from left to right as the recording time increases. To quantify the dependence of the SNR on T we also compute the regression equation, and we plot it in Figure 6. The regression equation is

$$(5.5) \quad \text{SNR} = \sqrt{0.0029T - 1.9133};$$

it shows that the SNR does linearly depend on the square root of recording time, as predicted by the theory presented in subsection 4.2 (see (4.13)).

SNR versus bandwidth. We apply here a treatment to the cross correlation in the Fourier domain in order to analyze the role of the bandwidth. More exactly, we apply a band-pass filter $H(f)$ to the recorded signals to retain only the frequency components centered at

Table 2

Configurations and SNR for 21 receivers and 200 sources. The spacing between receivers is $\lambda/2$. Note that here we use a different realization of noise sources compared to the results reported in Table 1 as for long recording times we considered only 21 receivers to reduce computational cost.

Recording time	SNR
$T = 1920 \mu\text{s}$	1.93
$T = 3840 \mu\text{s}$	3.04
$T = 5760 \mu\text{s}$	3.75
$T = 8640 \mu\text{s}$	4.81

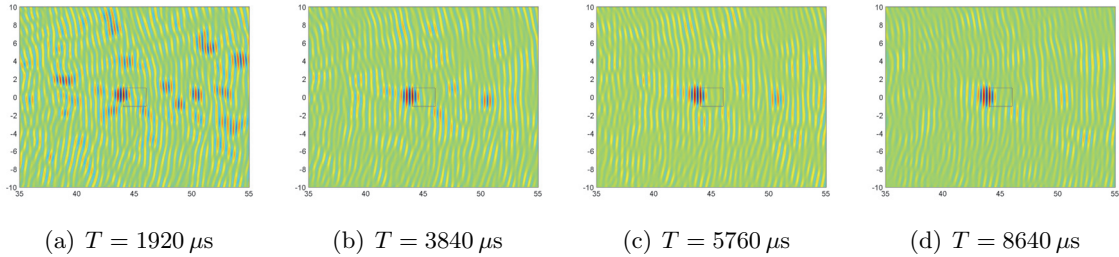


Figure 5. Daylight imaging with 200 sources and 21 receivers. The recording time is T .

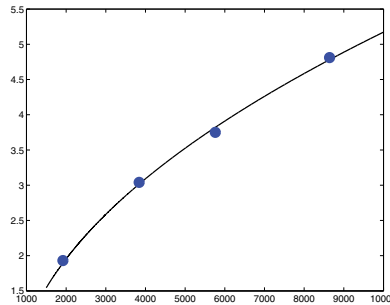


Figure 6. Plot of measured SNR versus recording time T (blue dots) and regression line (black line). There are 200 sources and 21 receivers. The spacing between receivers is $\lambda/2$.

the central frequency $f_0 = 500 \text{ kHz}$ with a bandwidth Δf : the filter has the form $H(f) = \mathbf{1}_{[f_0 - \Delta f/2, f_0 + \Delta f/2]}(|f|)$.

We plot in Figure 7 the Fourier transform of $u(t, \mathbf{x})$ for different positions of receivers (we plot only for the positive frequencies). One can see that the spectrum of the received signal is in the bandwidth $[0, 2f_0]$. Moreover, we observe that most information is concentrated for $0.5f_0 \leq |f| \leq 1.5f_0$ so that a band-pass filter with $\Delta f > f_0$ plays no role, but a band-pass filter with $\Delta f < f_0$ indeed removes low- and high-frequency components.

We record in Table 3 measured SNRs for different bandwidths Δf , and we plot the associated daylight images in Figure 8. As predicted by the theory, bandwidth affects both the image resolution and the SNR. The range resolution is c_0/B , and therefore as the effective bandwidth (here Δf) decreases the image becomes less focused in range. Loss of resolution is also accompanied by loss in SNR, and we observe that the amplitude of the ghosts in the

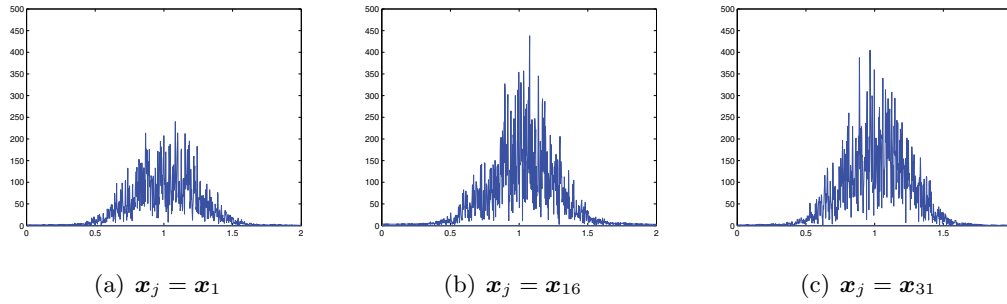


Figure 7. Plot of $\mathcal{F}(u)(\cdot, \mathbf{x}_j)$ versus f/f_0 .

Table 3

Configurations and SNR for 61 receivers and 200 sources. The spacing between receivers is $\delta = \lambda/2$. The recording time is $T = 480 \mu\text{s}$.

Δf	% of signal kept	SNR
$f_0/24$	33.90%	0.333
$f_0/12$	52.17%	0.70
$f_0/8$	61.09%	1.21
$f_0/6$	73.18%	1.48
$f_0/4$	84.83%	1.94
$f_0/2$	98.56%	3.63
f_0	100%	4.31

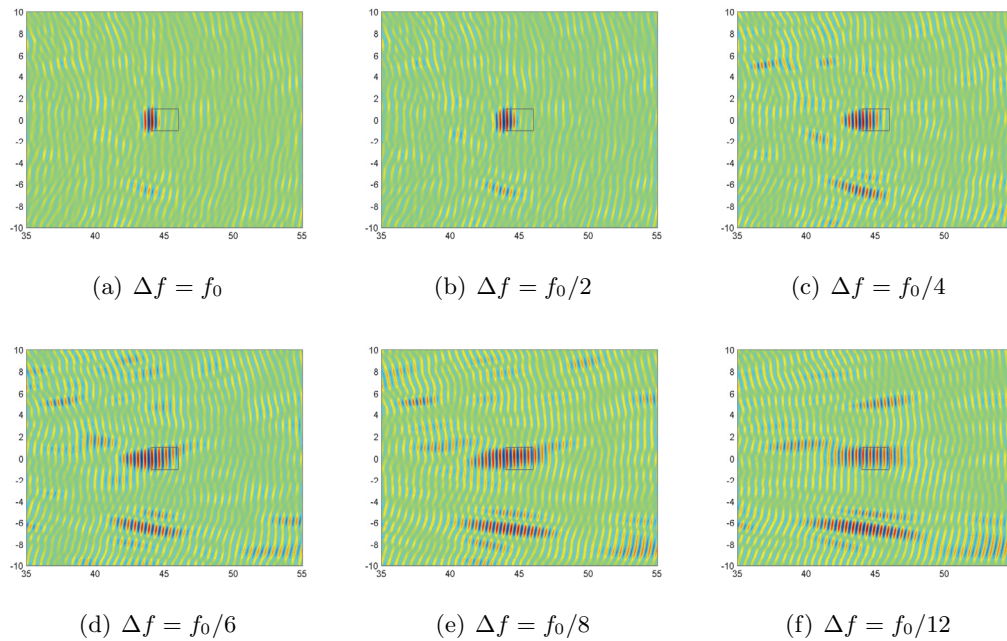


Figure 8. Daylight imaging with 200 sources and 61 receivers. The spacing between receivers is $\lambda/2$. We filter the data using the band-pass filter $H(f) = \mathbf{1}_{[f_0 - \Delta f/2, f_0 + \Delta f/2]}(|f|)$.

image increases as the bandwidth decreases.

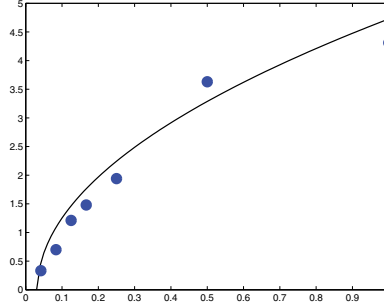


Figure 9. Plot of measured SNR (blue dots) as a function of the relative bandwidth $\Delta f/f_0$ and regression (black line). There are 200 sources and 61 receivers. The spacing between receivers is $\delta = \lambda/2$. The recording time is $T = 480 \mu\text{s}$.

We plot in Figure 9 the value of the SNR with respect to the bandwidth Δf (blue points) and the regression equation given by (5.6) (black line).

$$(5.6) \quad \text{SNR} = \sqrt{23.1\Delta f - 0.7402}.$$

SNR does linearly depend on the square root of bandwidth, as predicted by the theory proposed in subsection 4.2 (see (4.13)).

Conclusions. In this paper we have considered the problem of imaging by backpropagating or migrating cross correlations of passive noise recordings with an array of sensors. Motivated by the application of structural health monitoring, we have studied an imaging configuration where the sensors are located between the sources and the reflectors to be imaged (daylight illumination). The quality of the images obtained was analyzed in terms of both resolution and SNR. Our analysis shows that the important parameters for imaging are the following:

1. *The number of sensors N_R .* Both cross range resolution and SNR linearly improve with N_R .
2. *The bandwidth of the noise sources B .* Range resolution improves linearly with B , while the SNR is proportional to \sqrt{B} .
3. *The recording time T .* The SNR of the cross correlations, and therefore the SNR of the image as well, is proportional to \sqrt{T} .

Our numerical results are in very good agreement with our theoretical analysis.

Appendix A. Simulation of the noise source term. In this section, we give a precise sense to the noise sources $n(t, \mathbf{x})$. Given $N_S \in \mathbb{N}^*$, we take an i.i.d. random sequence of N_S points $(\mathbf{x}_s)_{1 \leq s \leq N_S}$ chosen uniformly in a given bounded domain Ω , and we take an i.i.d. random sequence of N_S functions in time $(f_s)_{1 \leq s \leq N_S}$. Let $g: \mathbb{R}^d \rightarrow \mathbb{R}$ be a positive radial decreasing function. We build the noise source $n(t, \mathbf{x})$ as

$$(A.1) \quad n(t, \mathbf{x}) = \frac{1}{\sqrt{N_S}} \sum_{s=1}^{N_S} f_s(t) g(\mathbf{x} - \mathbf{x}_s).$$

It is then easy to show the following.

Proposition A.1. *Assume that the family of functions $(f_s)_{1 \leq s \leq N_S}$ satisfies the two relations*

$$(A.2) \quad E \{f_s(t_1)f_s(t_2)\} = \mathbb{F}(t_1 - t_2),$$

$$(A.3) \quad E \{f_s(t_1)f_{s'}(t_2)\} = 0, \quad s' \neq s,$$

and the points $(\mathbf{x}_s)_{1 \leq s \leq N_S}$ are chosen independently and uniformly in the bounded domain Ω . Then

$$(A.4) \quad E \{n(t_1, \mathbf{x}_1)n(t_2, \mathbf{x}_2)\} = \mathbb{F}(t_1 - t_2) \frac{1}{|\Omega|} \int_{\Omega} g(\mathbf{x}_1 - \mathbf{x})g(\mathbf{x}_2 - \mathbf{x})d\mathbf{x},$$

where $|\Omega|$ is the volume of Ω .

Corollary A.2. *In relation (A.4), if $g = \delta$, then relation (2.3) is satisfied with*

$$(A.5) \quad K(\mathbf{x}) = \frac{1}{|\Omega|} \mathbf{1}_{\Omega}(\mathbf{x}).$$

Time-dependence of the noise source term. Here, we make precise how to build the random functions f_s in (A.1). To do so we use the classical representation formula for the Fourier transform of a stationary random signal $f_s(t)$ with power spectral density $\hat{\mathbb{F}}$:

$$\hat{f}_s(\omega) = \sqrt{\hat{\mathbb{F}}(\omega)}\hat{w}_s(\omega),$$

where $w_s(t)$ is a real white noise (a Gaussian process with mean zero and delta correlated covariance function $E \{w_s(t)w_s(t')\} = \delta(t - t')$). If the real white noises $(w_s)_{1 \leq s \leq N_S}$ are independent, then the functions $(f_s)_{1 \leq s \leq N_S}$ satisfy hypotheses (A.2), (A.3) of Proposition A.1.

Appendix B. Numerical computation of cross correlations. To numerically implement (3.1) in an efficient way, we first define $\tilde{u} : \mathbb{R} \rightarrow \mathbb{R}$, the extension of u to a $2T$ -periodic function, by

$$\tilde{u}(t, \mathbf{x}) = \begin{cases} u(t, \mathbf{x}) & \text{for } t \in [0, T], \\ 0 & \text{for } t \in [-T, 0]. \end{cases}$$

One can see that

$$(B.1) \quad C_T(\tau, \mathbf{x}_1, \mathbf{x}_2) = \frac{1}{T} \int_{-T}^T \tilde{u}(t, \mathbf{x}_1)\tilde{u}(t + \tau, \mathbf{x}_2)dt.$$

Assume now that we know $u(t, \mathbf{x}_1)$ and $u(t, \mathbf{x}_2)$ on a finite number N of discretization points $n\delta T$, with $0 \leq n < N$ and $\delta T = N^{-1}T$. If we introduce $t_n = (n - N)\delta T$ and call $\tilde{u}(\mathbf{x})_n$ the value of \tilde{u} at time t_n and at point \mathbf{x} , using a quadrature formula allows us to rewrite (B.1) as

$$(B.2) \quad C_T(\mathbf{x}_1, \mathbf{x}_2)_{N+k} = \frac{1}{N} \sum_{j=0}^{2N-1} \tilde{u}(\mathbf{x}_1)_j\tilde{u}(\mathbf{x}_2)_{j+k}.$$

Here, for the second index, we take the remainder in $\{0, \dots, 2N - 1\}$ modulo $2N$, and we use that $\tilde{u}(\mathbf{x}_1)_k = \tilde{u}(\mathbf{x}_2)_k = 0$ for $0 \leq k < N$.

To numerically compute (B.2), we use the discrete Fourier transform (DFT) as defined in the GNU Scientific Library [9],

$$(B.3) \quad \mathcal{F}(u)_n = \sum_{k=0}^{2N-1} u_k \exp\left(-2i\pi \frac{kn}{2N}\right).$$

We now apply the DFT on $(C_T(\mathbf{x}_1, \mathbf{x}_2)_k)$ and use the fact that \tilde{u} is real-valued to get

$$(B.4) \quad \mathcal{F}(C_T(\mathbf{x}_1, \mathbf{x}_2))_n = \frac{(-1)^n}{N} \overline{\mathcal{F}(\tilde{u}(\mathbf{x}_1))_n} \mathcal{F}(\tilde{u}(\mathbf{x}_2))_n.$$

We implemented the cross correlation computations as a part of Montjoie (<https://gforge.inria.fr/projects/montjoie/>). We use the Seldon library (<http://seldon.sourceforge.net/>) to deal with the various vectors we have to use. Our choice of implementing this in Montjoie is due to the fact that the numerical simulations of section 5 were done using this code. We use OpenMP (<http://openmp.org/wp/>) for parallelization of the program.

We have implemented both formulas (B.2) and (B.4); the first implementation is to check the validity of the second.

Appendix C. Passive sensor imaging. In this appendix we carry out the analysis of the statistical cross correlation $C^{(1)}$ when the background medium is homogeneous with background speed c_0 and there is a point reflector at \mathbf{z}_r . If we assume that the reflector is weak and small, then we can use the point interaction approximation for the Green's function [11]:

$$(C.1) \quad \hat{G}_r(\omega, \mathbf{x}, \mathbf{y}) = \hat{G}(\omega, \mathbf{x}, \mathbf{y}) + \frac{\omega^2}{c_0^2} \sigma_r l_r^2 \hat{G}(\omega, \mathbf{x}, \mathbf{z}_r) \hat{G}(\omega, \mathbf{z}_r, \mathbf{y}).$$

Here \hat{G} is the Green's function (2.4) of the background medium; that is, in the absence of a reflector, σ_r is the reflectivity of the point reflector, and l_r^2 is the effective scattering volume. The statistical cross correlation is given by

$$(C.2) \quad C^{(1)}(\tau, \mathbf{x}_1, \mathbf{x}_2) = C_0^{(1)}(\tau, \mathbf{x}_1, \mathbf{x}_2) + C_r^{(1)}(\tau, \mathbf{x}_1, \mathbf{x}_2),$$

where $C_0^{(1)}$ is the statistical cross correlation in the absence of a reflector, that is, (3.3) with the background Green's function (2.4). $C_r^{(1)}$ contains the additional terms due to the presence of the reflector:

$$(C.3) \quad \begin{aligned} C_r^{(1)}(\tau, \mathbf{x}_1, \mathbf{x}_2) = & \frac{\sigma_r l_r^2}{2\pi c_0^2} \iint d\mathbf{y} d\omega K(\mathbf{y}) \omega^2 \hat{\mathbb{F}}(\omega) \overline{\hat{G}(\omega, \mathbf{x}_1, \mathbf{y})} \hat{G}(\omega, \mathbf{x}_2, \mathbf{z}_r) \\ & \times \hat{G}(\omega, \mathbf{z}_r, \mathbf{y}) e^{-i\omega\tau} \\ & + \frac{\sigma_r l_r^2}{2\pi c_0^2} \iint d\mathbf{y} d\omega K(\mathbf{y}) \omega^2 \hat{\mathbb{F}}(\omega) \overline{\hat{G}(\omega, \mathbf{x}_1, \mathbf{z}_r)} \overline{\hat{G}(\omega, \mathbf{z}_r, \mathbf{y})} \\ & \times \hat{G}(\omega, \mathbf{x}_2, \mathbf{y}) e^{-i\omega\tau}, \end{aligned}$$

where we have retained only the terms of order $O(\sigma_r l_r^2)$ consistently with the Born or lowest-order scattering approximation.

In the high-frequency regime, that is, when the coherence time of the noise sources is smaller than the typical travel times, the statistical cross correlation has peaks at specific lag times that can be used for imaging. More exactly, the stationary phase analysis of $C_0^{(1)}$ shows that this cross correlation has a peak at the intersensor travel time $\mathcal{T}(\mathbf{x}_1, \mathbf{x}_2)$ [10]. The stationary phase analysis of $C_r^{(1)}$ when the noise sources are spatially localized and the sensors are between the sources and the reflectors (daylight illumination) shows that the singular components of the cross correlation $C_r^{(1)}$ are concentrated at lag times equal to (plus or minus) the sum of travel times $\mathcal{T}(\mathbf{x}_2, \mathbf{z}_r) + \mathcal{T}(\mathbf{x}_1, \mathbf{z}_r)$.

Proposition C.1. *In the daylight illumination configuration, in the high-frequency regime, the cross correlation $C_r^{(1)}$ has two singular contributions at lag times equal to plus or minus the sum of travel times $\mathcal{T}(\mathbf{x}_2, \mathbf{z}_r) + \mathcal{T}(\mathbf{x}_1, \mathbf{z}_r)$. The peak centered at plus the sum of travel times has the form*

$$(C.4) \quad C_r^{(1)}(\tau, \mathbf{x}_1, \mathbf{x}_2) = \frac{\sigma_r l_r^2}{16\pi} \frac{K_{\mathbf{x}_1, \mathbf{z}_r}}{|\mathbf{z}_r - \mathbf{x}_1|^{\frac{1}{2}} |\mathbf{z}_r - \mathbf{x}_2|^{\frac{1}{2}}} \mathbb{F}(\tau - [\mathcal{T}(\mathbf{x}_2, \mathbf{z}_r) + \mathcal{T}(\mathbf{x}_1, \mathbf{z}_r)]),$$

where $K_{\mathbf{x}, \mathbf{z}}$ is the power released by the noise sources along the ray starting from \mathbf{x} with the direction of $\mathbf{z} - \mathbf{x}$:

$$(C.5) \quad K_{\mathbf{x}, \mathbf{z}} = \int_0^\infty K\left(\mathbf{x} + \frac{\mathbf{x} - \mathbf{z}}{|\mathbf{x} - \mathbf{z}|} l\right) dl.$$

The peak centered at minus the sum of travel times has the form

$$(C.6) \quad C_r^{(1)}(\tau, \mathbf{x}_1, \mathbf{x}_2) = -\frac{\sigma_r l_r^2}{16\pi} \frac{K_{\mathbf{x}_2, \mathbf{z}_r}}{|\mathbf{z}_r - \mathbf{x}_1|^{\frac{1}{2}} |\mathbf{z}_r - \mathbf{x}_2|^{\frac{1}{2}}} \mathbb{F}(\tau + [\mathcal{T}(\mathbf{x}_2, \mathbf{z}_r) + \mathcal{T}(\mathbf{x}_1, \mathbf{z}_r)]).$$

Note that $K_{\mathbf{x}_j, \mathbf{z}_r}$ is not zero only if the ray going from \mathbf{z}_r to \mathbf{x}_j extends into the source region, which is the daylight illumination configuration.

Proof. We consider the high-frequency regime in which $\mathbb{F}(\tau) = F(\tau/\varepsilon)$, where ε is a small parameter that characterizes the ratio between the coherence time of the noise sources and the typical travel time. We consider the first term in the right-hand side of (C.3):

$$C_{r,1}^{(1)}(\tau, \mathbf{x}_1, \mathbf{x}_2) = \frac{\sigma_r l_r^2}{2\pi c_0^2 \varepsilon^2} \iint d\mathbf{y} d\omega K(\mathbf{y}) \omega^2 \hat{F}(\omega) \overline{\hat{G}}\left(\frac{\omega}{\varepsilon}, \mathbf{x}_1, \mathbf{y}\right) \hat{G}\left(\frac{\omega}{\varepsilon}, \mathbf{x}_2, \mathbf{z}_r\right) \\ \times \hat{G}\left(\frac{\omega}{\varepsilon}, \mathbf{z}_r, \mathbf{y}\right) e^{-i\frac{\omega\tau}{\varepsilon}}.$$

We use the asymptotic behavior of the Hankel function

$$H_0^{(1)}(r) \stackrel{r \gg 1}{\simeq} \frac{2^{\frac{1}{2}}}{\pi^{\frac{1}{2}} r^{\frac{1}{2}}} \exp\left(ir - i\frac{\pi}{4}\right),$$

which gives

$$C_{r,1}^{(1)}(\tau, \mathbf{x}_1, \mathbf{x}_2) = \frac{\sigma_r l_r^2 e^{i\pi/4}}{2^{\frac{1}{2}} \pi^{\frac{5}{2}} c_0^{\frac{1}{2}} \varepsilon^{\frac{1}{2}}} \iint d\mathbf{y} d\omega \frac{\omega^{\frac{1}{2}} \hat{F}(\omega) K(\mathbf{y})}{[|\mathbf{y} - \mathbf{x}_1| |\mathbf{y} - \mathbf{z}_r| |\mathbf{z}_r - \mathbf{x}_2|]^{\frac{1}{2}}} e^{i\frac{\omega}{\varepsilon} \mathcal{T}_0(\mathbf{y})},$$

where the rapid phase is

$$\mathcal{T}_0(\mathbf{y}) = -\mathcal{T}(\mathbf{y}, \mathbf{x}_1) + \mathcal{T}(\mathbf{y}, \mathbf{z}_r) + \mathcal{T}(\mathbf{z}_r, \mathbf{x}_2) - \tau.$$

The dominant contribution comes from the stationary points (ω, \mathbf{y}) that satisfy

$$\nabla_{\mathbf{y}}(\omega\mathcal{T}_0(\mathbf{y})) = \mathbf{0}, \quad \partial_{\omega}(\omega\mathcal{T}_0(\mathbf{y})) = 0,$$

which reads

$$\nabla_{\mathbf{y}}\mathcal{T}(\mathbf{y}, \mathbf{x}_1) = \nabla_{\mathbf{y}}\mathcal{T}(\mathbf{y}, \mathbf{z}_r), \quad \tau = -\mathcal{T}(\mathbf{y}, \mathbf{x}_1) + \mathcal{T}(\mathbf{y}, \mathbf{z}_r) + \mathcal{T}(\mathbf{z}_r, \mathbf{x}_2).$$

The first condition imposes that \mathbf{x}_1 and \mathbf{z}_r are on the same ray issued from \mathbf{y} . The second condition then reads $\tau = \pm\mathcal{T}(\mathbf{z}_r, \mathbf{x}_1) + \mathcal{T}(\mathbf{z}_r, \mathbf{x}_2)$, with the sign $+$ (resp., $-$) if $\mathbf{y} \rightarrow \mathbf{x}_1 \rightarrow \mathbf{z}_r$ (resp., $\mathbf{y} \rightarrow \mathbf{z}_r \rightarrow \mathbf{x}_1$). For the daylight illumination configuration we have $\mathbf{y} \rightarrow \mathbf{x}_1 \rightarrow \mathbf{z}_r$. Using the change of variable $\mathbf{y} \in \mathbb{R}^2 \rightarrow (s, u) \in \mathbb{R}^+ \times \mathbb{R}$,

$$\mathbf{y} = \mathbf{x}_1 + |\mathbf{x}_1 - \mathbf{z}_r|(s\mathbf{e}_1 + \varepsilon^{\frac{1}{2}}u\mathbf{e}_2),$$

with $\mathbf{e}_1 = (\mathbf{x}_1 - \mathbf{z}_r)/|\mathbf{x}_1 - \mathbf{z}_r|$ and $\mathbf{e}_2 \perp \mathbf{e}_1$, and the parametrization $\tau = \mathcal{T}(\mathbf{x}_1, \mathbf{z}_r) + \mathcal{T}(\mathbf{x}_2, \mathbf{z}_r) + \varepsilon\tau_1$, we find

$$\mathcal{T}_0(\mathbf{y}) = -\varepsilon \frac{|\mathbf{x}_1 - \mathbf{z}_r|}{2c_0s(1+s)}u^2 - \varepsilon\tau_1 + O(\varepsilon^2),$$

and therefore

$$C_{r,1}^{(1)}(\tau, \mathbf{x}_1, \mathbf{x}_2) = \frac{\sigma_r l_r^2}{2^5 \pi^2} \iint ds d\omega \frac{\hat{F}(\omega) K(\mathbf{x}_1 + |\mathbf{x}_1 - \mathbf{z}_r|s\mathbf{e}_1)}{|\mathbf{z}_r - \mathbf{x}_1|^{-\frac{1}{2}} |\mathbf{z}_r - \mathbf{x}_2|^{\frac{1}{2}}} e^{-i\omega\tau_1},$$

where we have used the identity

$$\int e^{-i\frac{u^2}{2}} du = \sqrt{2\pi} e^{-i\frac{\pi}{4}}.$$

The second term in (C.3) can be addressed in the same way, which gives the desired result. ■

REFERENCES

- [1] C. BARDOS, J. GARNIER, AND G. PAPANICOLAOU, *Identification of Green's functions singularities by cross-correlation of noisy signals*, Inverse Problems, 24 (2008), 015011.
- [2] L. BORCEA, G. PAPANICOLAOU, AND C. TSOGKA, *A resolution study for imaging and time reversal in random media*, Contemp. Math., 333 (2003), pp. 63–77.
- [3] L. BORCEA, G. PAPANICOLAOU, AND C. TSOGKA, *Adaptive interferometric imaging in clutter and optimal illumination*, Inverse Problems, 22 (2006), pp. 1405–1436.
- [4] M. BORN AND E. WOLF, *Principle of Optics*, Cambridge University Press, Cambridge, UK, 1999.
- [5] M. CAMPILLO, H. SATO, N. M. SHAPIRO, AND R. D. VAN DER HILST, *New developments on imaging and monitoring with seismic noise*, C. R. Geoscience, 343 (2011), pp. 487–495.
- [6] Y. COLIN DE VERDIÈRE, *Semiclassical analysis and passive imaging*, Nonlinearity, 22 (2010), pp. R45–R75.

- [7] T. L. DUVAL, S. M. JEFFERIES, J. W. HARVET, AND M. A. POMERANTZ, *Time-distance helioseismology*, *Nature*, 362 (1993), pp. 430–432.
- [8] M. FRIGO AND S. G. JOHNSON, *The design and implementation of FFTW3*, *Proc. IEEE*, 93 (2005), pp. 216–231.
- [9] M. GALASSI, J. DAVIES, J. THEILER, B. GOUGH, G. JUNGMAN, M. BOOTH, AND F. ROSSI, *GNU Scientific Library Reference Manual, Revised Second Edition (v1.8)*, Network Theory Ltd, Godalming, UK, 2006.
- [10] J. GARNIER AND G. PAPANICOLAOU, *Passive sensor imaging using cross correlations of noisy signals in a scattering medium*, *SIAM J. Imaging Sci.*, 2 (2009), pp. 396–437.
- [11] J. GARNIER AND G. PAPANICOLAOU, *Resolution analysis for imaging with noise*, *Inverse Problems*, 26 (2010), 074001.
- [12] P. GOUÉDARD, L. STEHLY, F. BRENGUIER, M. CAMPILLO, Y. COLIN DE VERDIÈRE, E. LAROSE, L. MARGERIN, P. ROUX, F. J. SÁNCHEZ-SESMA, N. M. SHAPIRO, AND R. L. WEAVER, *Cross-correlation of random fields: Mathematical approach and applications*, *Geophys. Prospect.*, 56 (2008), pp. 375–393.
- [13] K. G. SABRA, P. GERSTOFT, P. ROUX, W. A. KUPERMAN, AND M. C. FEHLER, *Extracting time domain Green's function estimates from ambient seismic noise*, *Geophys. Res. Lett.*, 32 (2005), L03310.
- [14] K. G. SABRA, A. SRIVASTAVA, F. LANZA DI SCALEA, I. BARTOLI, P. RIZZO, AND S. CONTI, *Structural health monitoring by extraction of coherent guided waves from diffuse fields*, *J. Acoust. Soc. Am.*, 123 (2008), pp. EL8–EL13.
- [15] N. M. SHAPIRO, M. CAMPILLO, L. STEHLY, AND M. RITZWOLLER, *High resolution surface wave tomography from ambient seismic noise*, *Science*, 307 (2005), pp. 1615–1618.
- [16] R. SNIEDER, *Extracting the Green's function from the correlation of coda waves: A derivation based on stationary phase*, *Phys. Rev. E*, 69 (2005), 046610.
- [17] R. SNIEDER AND K. WAPENAAR, *Imaging with ambient noise*, *Phys. Today*, 307 (2010), pp. 1615–1618.
- [18] K. WAPENAAR, D. DRAGANOV, R. SNIEDER, X. CAMPMAN, AND A. VERDEL, *Tutorial on seismic interferometry. Part 1: Basic principles and applications*, *Geophysics*, 75 (2010), pp. 75A195–75A209.
- [19] K. WAPENAAR, E. SLOB, R. SNIEDER, AND A. CURTIS, *Tutorial on seismic interferometry. Part 2: Underlying theory and new advances*, *Geophysics*, 75 (2010), pp. 75A211–75A227.
- [20] R. L. WEAVER AND O. I. LOBKIS, *Ultrasonics without a source: Thermal fluctuation correlations at MHz frequencies*, *Phys. Rev. Lett.*, 87 (2001), 134301.